Supplementary Information:*In situ* X-ray Imaging of Segregation and Mixing in PtPd Core-Shell Nanoparticles under Methane Oxidation Conditions

Lydia J. Bachmann[1,2], Jagrati Dwivedi[1], Dmitry Lapkin[3,4], Bihan Wang[3], Jan-Christian Schober[1,2], Gerard N. Hinsley[3], Sarah Bernart[5,7], Kuan Hoon Ngoi[3], Rustam Rysov[3,6], Arti Dangwal Pandey[1], Thomas F. Keller[1,2], Ivan A. Vartanyants[3], Andreas Stierle[1,2*]

[1]Centre for X-ray and Nano Science CXNS, Deutsches Elektronen-Synchrotron DESY, Notkestr. 85, Hamburg, 22607, Germany.
[2]Department of Physics, University of Hamburg, Notkestraße 9-11, Hamburg, 22607, Germany.
[3]Deutsches Elektronen-Synchrotron DESY, Notkestr. 85, Hamburg, 22607, Germany.
[4]Current Address: Institute of Applied Physics, University of Tübingen, Tübingen, 72076, Germany.
[5]Institute of Catalysis Research and Technology, Karlsruhe Institute of Technology, Hermann-von-Helmholtz-Platz 1, Eggenstein-Leopoldshafen, 76344, Germany.
[6]Current Address: European X-ray Free-Electron Laser Facility, Holzkoppel 4, Schenefeld, 22869, Germany.
[7]Current Address: Inorganic Materials and Catalysis, Eindhoven University of Technology, 5600 MB Eindhoven, Netherlands.

*Corresponding author(s). E-mail(s): andreas.stierle@desy.de;

S1 EBL pattern

Figure S1 shows the EBL pattern on the example of Sample-670. Sample-150 was prepared with a similar pattern.

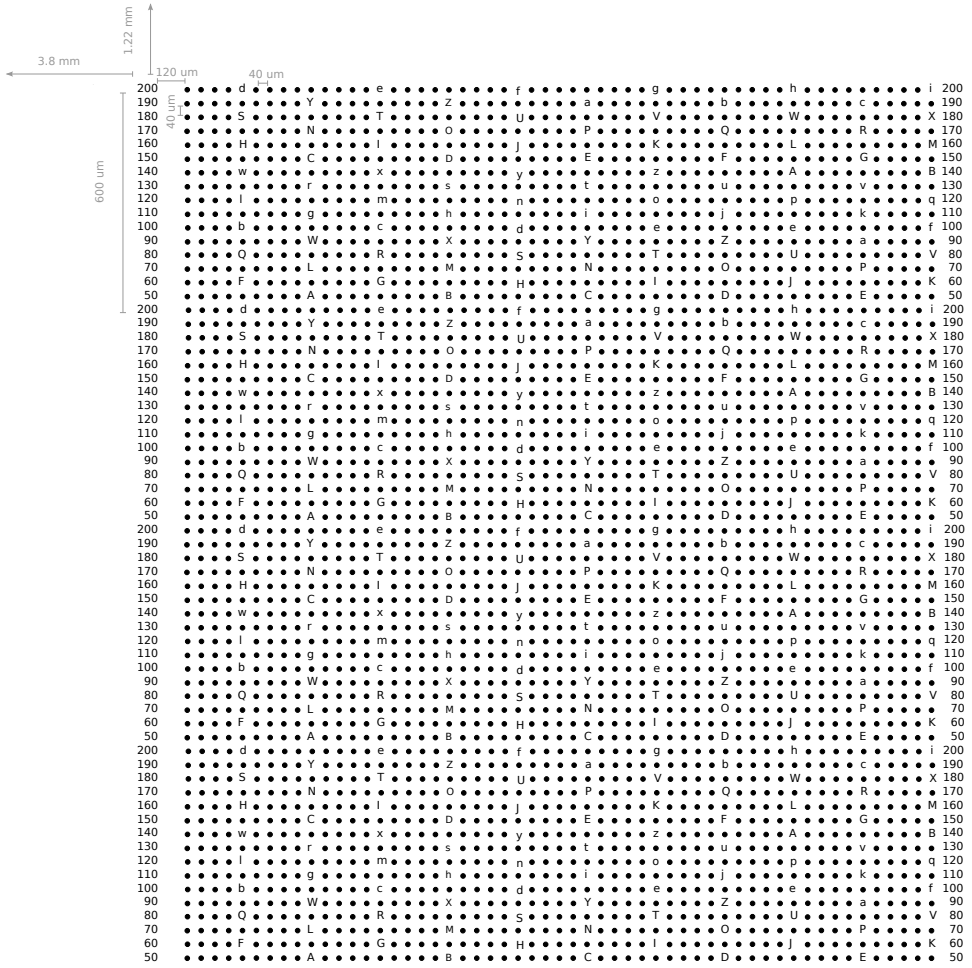

(a)

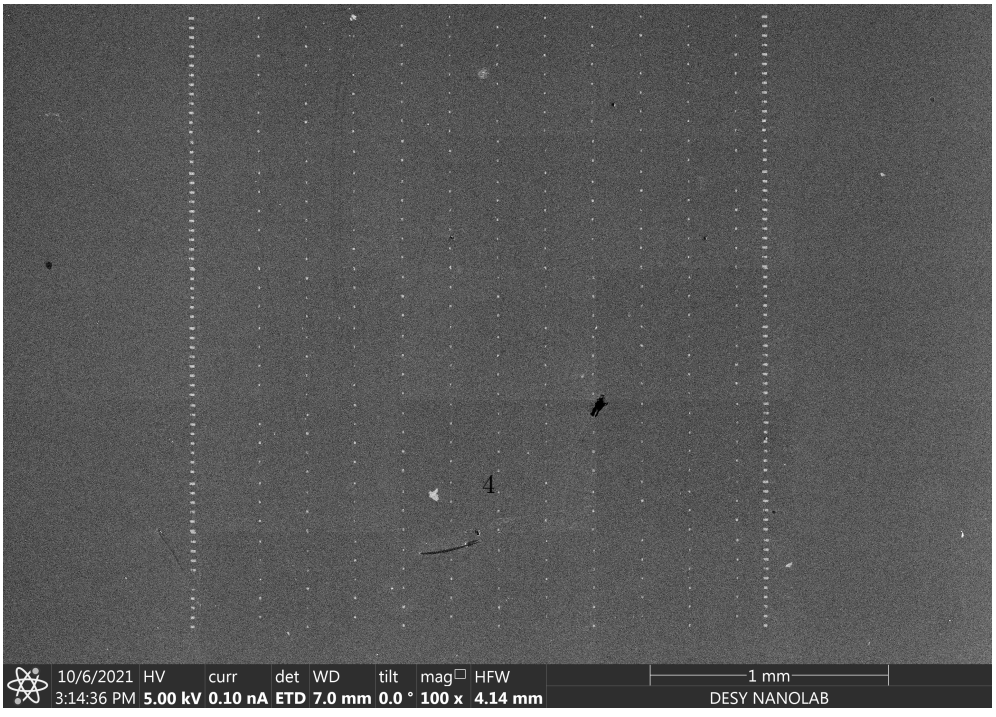

(b)

Fig. S1 EBL pattern of Sample-670
a) Sketch of the EBL pattern of Sample-670 with the markers (a-z, A-Z and 50-200) and nanodots (indicated by a black dot) together with the distances (in gray) and b) overview of that pattern on the sample in SEM.

S2 Nominal thickness

Since the two samples were prepared around one year after each other, two different calibration samples were used. These calibration samples are needed to calculate the deposition rate and therefore the thickness of the evaporated Pd layers.

For Sample-150 the calibration sample was prepared for t_{calibr} =38 min with an average flux of f_{calibr} = 10.6±2 nA. The evaporated material was analyzed by X-ray reflectivity (XRR), measuring a thickness of d_{calibr} = 25.5±0.23 Å and a coverage of Φ_{calibr} = 0.797 ± 0.006. With this the deposition rate s was calculated by $s = d_{\text{calibr}} \cdot \Phi_{\text{calibr}}/(t_{\text{calibr}} \cdot f_{\text{calibr}})$. Using this deposition rate, the nominal thickness d_{nom} on Sample-150 can be calculated to $d_{\text{nom}} = s \cdot t_{\text{S-150}} \cdot f_{\text{S-150}}$ = 17.28±7.53 Å = 1.7± 0.7 nm with the flux $f_{\text{S-150}}$ = 215 nA and the time $t_{\text{S-150}}$ =13 min.

For Sample-670 the calibration sample was prepared for t_{calibr2} =106 min with an average flux of f_{calibr2} = 21±2 nA. The evaporated material was analyzed by XRR with a two layer fit with a thickness d_1 = 12.1±3 Å, coverage Φ_1 = 0.62, thickness d_2 = 57.8±0.4 Å and coverage Φ_2 = 0.64. With this the deposition rate s was calculated by $s = (d_1 \cdot \Phi_1 + d_2 \cdot \Phi_2)/(t_{\text{calibr2}} \cdot f_{\text{calibr2}})$. Thus, the nominal thickness d_{nom} on Sample-670 is $d_{\text{nom}} = s \cdot t_{\text{S-670}} \cdot f_{\text{S-670}}$ = 48.9±1.6 Å= 4.9±0.2 nm with the average flux $f_{\text{S-670}}$ = 40±5 nA for a time $t_{\text{S-670}}$ =61 min.

S3 Diffusion length

Sample-150 was overgrown with Pd for 13 min at 150 °C and Sample-670 for 1 h at 670 °C. These different temperatures and times lead to different diffusion of the Pd into the Pt. To estimate the diffusion of the Pd into the Pt NPs, the diffusion length can be calculated.

Therefore, the diffusion coefficient was calculated using:

$$D = D_0 e^{\frac{-E}{R \cdot T}} \tag{S1}$$

with the experimental prefactor $D_0 = 0.33 \times 10^{-4}$ $\mathrm{m^2\,s^{-1}}$,[9] the activation energy $E = 324$ $\mathrm{kJ\,mol^{-1}}$,[4] the gas constant $R = 8.3$ $\mathrm{J\,mol^{-1}\,K^{-1}}$ and the temperature T in K. From the diffusion coefficient the diffusion length of each sample was calculated using $l = \sqrt{D \cdot t}$, with the time t in seconds. The diffusion during the cool down after the overgrowth of the sample was neglected, resulting in diffusion lengths of 1.5×10^{-12} nm for Sample-150 and 0.4 nm for Sample-670.

S4 Nominal volume fraction

For both NPs the nominal composition in vol % was estimated by $V_{\mathrm{Pd}}/V_{\mathrm{tot}} \cdot 100$ from the total NP volume V_{tot} and the volume V_{Pd} of the overgrown Pd. Therefore, the NPs were assumed to have a hexagonal base and top, as shown in Figure S2. Thus the volumes V_{Pd} and V_{tot} can be calculated by $V = A \cdot h$ using the nominal Pd thickness as height h of the Pd volume and the measured height in the AFM for the total NP volume. Thereby, the area of each NP was calculated by $A = 2 \cdot \sqrt{3} r^2$ with the diameter r as measured in the respective SEM images. Note, that this is only a rough estimation, neglecting the side facets of the NP.

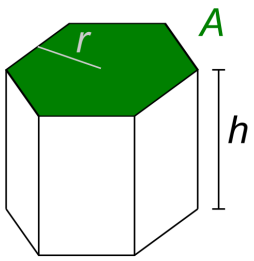

Fig. S2 Simplified sketch of a nanoparticle as used for estimating the nominal composition
With the height h, the radius r and the surface area (green) A.

S5 Height determination from intensity distribution around Bragg peak

The size of the NPs can be determined from the three dimensional (3D) diffraction pattern in reciprocal space. Therefore, all detector images of one dataset were flatfield corrected, stacked and hot pixels were removed. Then, the resulting 3D diffraction pattern was transformed into the laboratory coordinate system. An example of such a 3D diffraction pattern is shown in Figure S3a). From the line-profile along the fringes in Qz-direction, perpendicular to the NP top facet, one can calculate the distances dQ between the minima (green dots in Figure S3b)), which allows to determine the height h of the nanoparticle by the following equation:

$$h = \frac{2\pi}{\overline{dQ}} = \frac{2\pi}{\frac{1}{n}\sum dQ} \tag{S2}$$

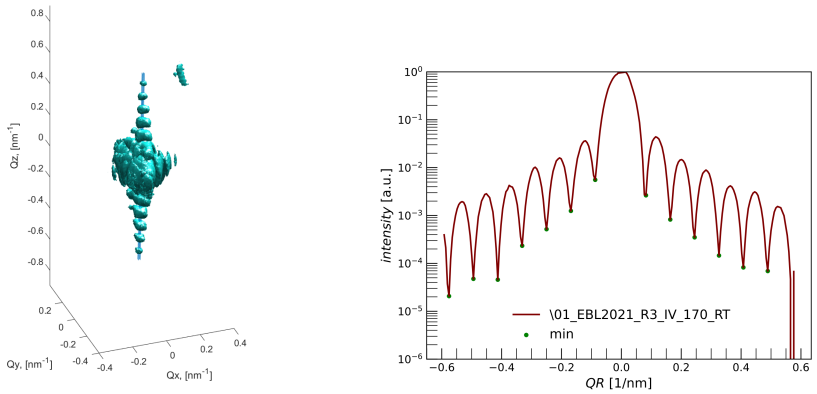

(a) (b)

Fig. S3 Example line profile through the intensity distribution around a Bragg peak a) 3D logarithmic intensity distribution with an isosurface value of 0.3 around the Bragg peak in the laboratory coordinate system at the initial state for Sample-670. b) Normalized line profile through the intensity distribution along the blue lines in a) .

Since it is averaged over all n distances dQ with the standard deviation $s_{\overline{\mathrm{dQ}}}$, the error for the height is:

$$s_{\mathrm{h}} = \frac{2\pi}{\overline{dQ}^2} s_{\overline{\mathrm{dQ}}} \tag{S3}$$

To reduce statistical errors and to avoid gaps in the profile due to removed pixels, each line-profile is averaged over 5 voxels and normalized, while taking into account that the fringes are not exactly parallel to Qz.

S6 Phase retrieval algorithm sequences

Table S1 contains the phase retrieval algorithm sequences for all datasets obtained on Sample-150. The corresponding region of interests (ROIs) used for the reconstructions are displayed in Figure S4. Table S2 contains the same information about Sample-670 and their corresponding ROIs are displayed in Figure S5 and Figure S6. Even after choosing the best from over 250 single reconstructions, the result could not be improved for Sample-150 dataset 3, 5 and 7 and Sample-670 datset 21 (for the latter an average over 4 instead of 10 reconstructions is used for further analysis). Datasets 4, 6 and 10 of Sample-150 could not be reconstructed.

Table S1 Overview over the used sequences to reconstruct the datasets collected on Sample-150. The achieved voxel size depends mainly on the size of the used ROIs, which are displayed in Figure S4.

dataset number	cycles	reconstruction methods	shrink wrap	voxel size $x \times y \times z$ [nm]
1	3	300 HIO + 300 ER	0.2	$7.1 \times 5.6 \times 5.6$
2	3	300 HIO + 300 ER	0.2	$7.1 \times 3.7 \times 3.6$
3	3	300 DM + 300 ER	0.17	$7.1 \times 6.7 \times 6.6$
4	-	not reconstructable	-	-
5	3	300 DM + 300 ER	0.15	$6.8 \times 3.5 \times 3.5$
6	-	dataset incomplete	-	-
7	3	300 DM + 300 ER	0.1	$7.1 \times 3.2 \times 3.2$
8	3	300 HIO + 300 ER	0.07	$7.0 \times 5.6 \times 5.5$
9	3	300 HIO + 300 ER	0.1	$9.0 \times 3.5 \times 3.5$
10	-	not reconstructable	-	-
11	3	300 HIO + 300 ER	0.07	$7.5 \times 3.4 \times 3.4$
12	3	300 HIO + 300 ER	0.1	$7.1 \times 3.3 \times 3.3$
13	3	300 DM + 300 ER	0.2	$7.0 \times 3.3 \times 3.3$
14	3	300 HIO + 300 ER	0.2	$7.0 \times 3.1 \times 3.1$

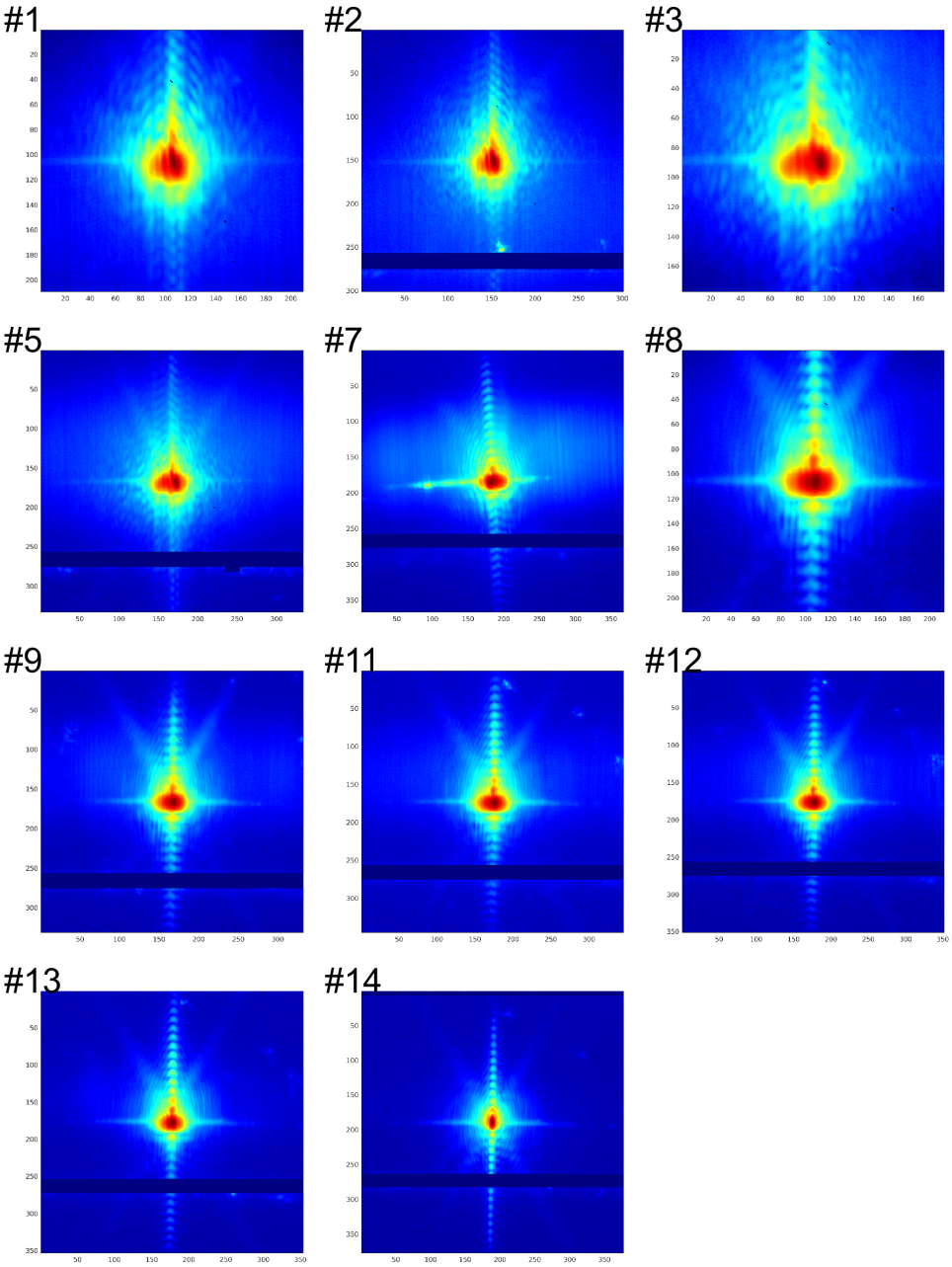

Fig. S4 ROI of stacked datasets on Sample-150
Overview over all used ROIs used to reconstruct the datasets. Dataset 4 and 10 were not reconstructable and dataset 6 was incomplete, and are therefore not shown.

Table S2 Overview over the used sequences to reconstruct the datasets collected on Sample-670. The achieved voxel size depends on the size of the used ROIs, which are displayed in Figure S5 and Figure S6 and the range of the scanned angle.

dataset number	cycles	reconstruction methods	shrink wrap	voxel size $x \times y \times z$ [nm]
1	3	300 HIO + 300 ER	0.2	$5.7 \times 5.2 \times 5.2$
2	3	300 HIO + 300 ER	0.2	$5.7 \times 4.6 \times 4.6$
3	3	300 HIO + 300 ER	0.2	$4.6 \times 4.6 \times 4.6$
4	3	300 HIO + 300 ER	0.2	$4.7 \times 4.6 \times 4.7$
5	3	300 HIO + 300 ER	0.2	$4.6 \times 4.7 \times 4.7$
6	3	300 HIO + 300 ER	0.2	$4.7 \times 4.7 \times 4.7$
7	3	300 HIO + 300 ER	0.2	$4.5 \times 4.7 \times 4.6$
8	3	300 HIO + 300 ER	0.2	$4.6 \times 4.8 \times 4.8$
9	3	300 DM + 300 ER	0.2	$4.8 \times 5.1 \times 5.0$
10	3	300 HIO + 300 ER	0.2	$4.6 \times 5.0 \times 5.0$
11	4	300 DM + 300 ER	0.2	$4.6 \times 4.6 \times 4.6$
12	3	300 DM + 300 ER	0.2	$4.8 \times 4.6 \times 4.6$
13	3	300 HIO + 300 ER	0.2	$4.9 \times 4.6 \times 4.6$
14	3	300 HIO + 300 ER	0.2	$4.8 \times 4.7 \times 4.7$
15	4	300 DM + 300 ER	0.2	$4.6 \times 4.8 \times 4.7$
16	3	300 DM + 300 ER	0.2	$4.6 \times 4.9 \times 4.8$
17	4	300 DM + 300 ER	0.2	$4.7 \times 4.9 \times 4.9$
18	3	300 DM + 300 ER	0.2	$4.7 \times 4.6 \times 4.6$
19	4	300 DM + 300 ER	0.2	$4.8 \times 4.8 \times 4.8$
20	3	300 DM + 300 ER	0.2	$4.6 \times 5.2 \times 5.3$
21	3	300 HIO + 300 ER	0.2	$4.8 \times 4.7 \times 4.6$
22	4	300 DM + 300 ER	0.2	$4.9 \times 5.2 \times 5.1$
23	4	300 DM + 300 ER	0.2	$4.8 \times 4.8 \times 4.7$
24	4	300 DM + 300 ER	0.2	$4.6 \times 4.8 \times 4.8$
25	3	300 HIO + 300 ER	0.2	$4.9 \times 5.1 \times 5.1$

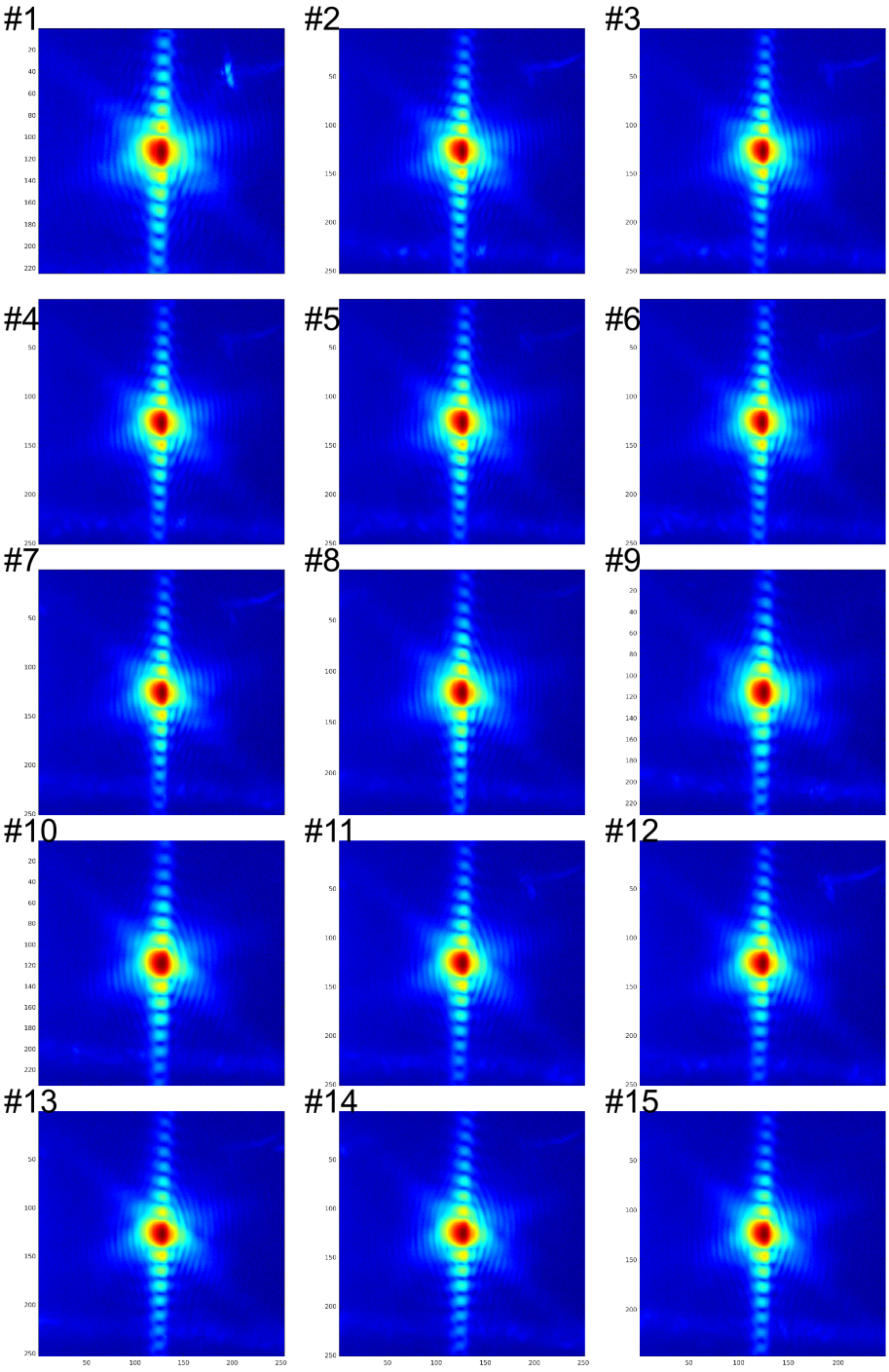

Fig. S5 ROI of stacked datasets on Sample-670
Overview over the first half of the used ROIs used to reconstruct the datasets.

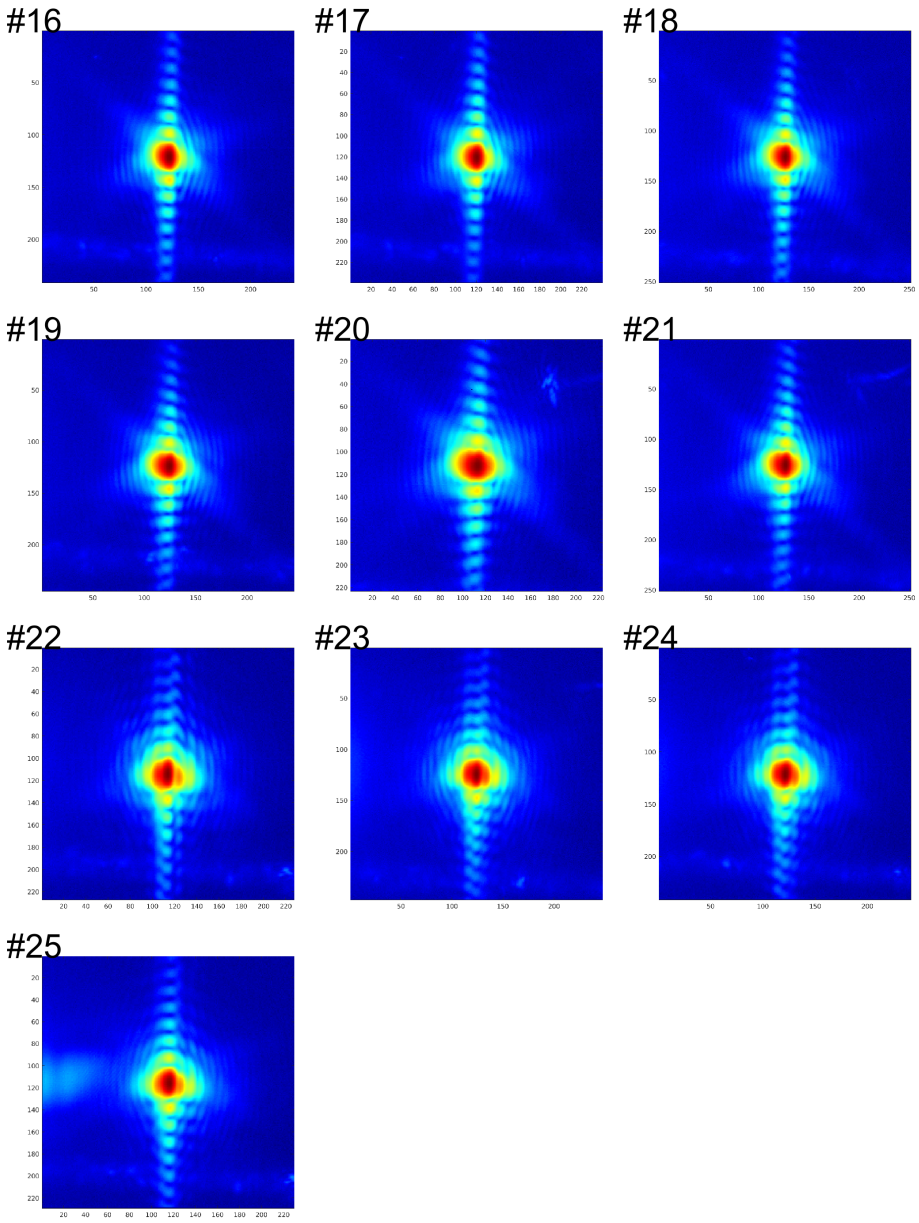

Fig. S6 ROI of stacked datasets on Sample-670
Overview over the second half of the used ROIs used to reconstruct the datasets.

S7 Lattice constant and strain from Bragg peak position

The lattice spacing a_{NP} is calculated by

$$a_{\mathrm{NP}} = \frac{\sqrt{h^2 + k^2 + l^2} \cdot \lambda}{2 \cdot \sin(\Theta)} \tag{S4}$$

with the wavelength λ and the 111 reflection (thus $h = k = l = 1$). The angle between the incident and the scattered beam 2Θ was calculated from the out-of-plane detector angle δ and the in-plane detector angle γ, taking the sample-detector distance SDD and the in- and out-of-plane distance on the detector between the Bragg peak and the direct beam position $d_{\text{in-plane}}$ and $d_{\text{out-of-plane}}$ into account:

$$2\Theta = \arccos(\cos(\delta + \arctan(\frac{d_{\text{out-of-plane}}}{SDD})) \cdot \cos(\gamma + \arctan(\frac{d_{\text{in-plane}}}{SDD}))) \tag{S5}$$

The lattice constants for all datasets are listed in Table S3 and Table S4. Assuming that we can determine the position of the Bragg peak in the detector image by $\pm$ 1 px in in-plane and out-of-plane directions leads to an error on the lattice constant of 1×10^{-3}Å for all datasets on both samples.

Table S3 Overview over the lattice constant of all datasets on Sample-150, including the corresponding temperatures and gas conditions.

dataset number	a_{NP} [Å]	T [°C]	gas cond.
1	3.920	RT	Ar
2	3.920	RT	Ar
3	3.932	320	Ar
4	-	320	Ar
5	3.932	320	H2 treatment
6	-	470	Ar
7	3.937	470	Ar
8	3.920	RT	Ar
9	3.932	320	Ar
10	3.938	470	Ar
11	3.937	470	methane ox.
12	3.939	520	methane ox.
13	3.942	560	methane ox.
14	3.944	620	methane ox.

We defined the strain ϵ by

$$\epsilon = (d - d_{NP})/d_{NP} \times 100 \tag{S6}$$

d is thereby the d-spacing in the direction of the measured Bragg peak, thus $d = a/\sqrt{3}$ for the 111 Bragg Peak. With this the strain for a region with pure Pd at 680 °C was calculated for Sample-670 to:

$$\epsilon = (a_{Pd} - a_{NP})/a_{NP} \times 100 = (-0.46 \pm 0.02)\% \tag{S7}$$

with $a_{NP} = 3.944 \pm 0.001$ Å from the Bragg peak center for dataset 22. The lattice constants of Pd and Pt at several temperatures are displayed in Table S5. To include the thermal expansion, the lattice constant of Pt was calculated by

Table S4 Overview over the lattice constant for all datasets on Sample-670, including the corresponding temperatures and gas conditions.

dataset number	a_{NP} [Å]	T [°C]	gas cond.
1	3.920	RT	Ar
2	3.931	320	Ar
3	3.931	320	methane ox.
4	3.930	320	methane ox.
5	3.930	320	methane ox.
6	3.930	320	methane ox.
7	3.935	440	methane ox.
8	3.938	490	methane ox.
9	3.942	530	methane ox.
10	3.940	550	methane ox.
11	3.931	320	Ar
12	3.930	320	methane ox.
13	3.934	410	methane ox.
14	3.935	440	methane ox.
15	3.937	490	methane ox.
16	3.939	530	methane ox.
17	3.939	550	methane ox.
18	3.931	320	Ar
19	3.938	510	Ar
20	3.920	RT	Ar
21	3.930	320	methane ox.
22	3.944	680	methane ox.
23	3.930	320	methane ox.
24	3.940	570	methane ox.
25	3.944	680	methane ox.

$$\begin{aligned} a_{\mathrm{Pt}}(T) =& ((7.08788 \times 10^{-6} \cdot T + 5.24850 \times 10^{-9} \cdot T^2 - 6.69487 \times 10^{-12} \cdot T^3 \\ &+ 5.70500 \times 10^{-15} \cdot T^4 - 2.36906 \times 10^{-18} \cdot T^5 + 3.95580 \times 10^{-22} \cdot T^6 \\ &- 2.39745 \times 10^{-3}) - 1/3 \cdot e^{1.32-17523/T}) \cdot a_{\mathrm{Pt,RT}} + a_{\mathrm{Pt,RT}} \end{aligned} \tag{S8}$$

as described in [2]. The lattice constant of Pd was calculated by

$$\begin{aligned} a_{\mathrm{Pd}}(T) =& (-3.67831 \times 10^{-3} + 1.10122 \times 10^{-5} \cdot T + 2.69121 \times 10^{-9} \cdot T^2 \\ &-2.25680 \times 10^{-13} \cdot T^3 + 6.58134 \times 10^{-2}/T) \cdot a_{\mathrm{Pd,RT}} + a_{\mathrm{Pd,RT}} \end{aligned} \tag{S9}$$

as described in [3].

Table S5 Overview over the lattice constant of Pt and Pd at selected temperatures.

temperature	a_{Pt} [Å]	a_{Pd} [Å]
RT	3.923	3.890
320 °C	3.935	3.905
560 °C	3.944	3.919
620 °C	3.946	3.922
680 °C	3.949	3.926

S8 Histogram of strain values

Figure S8 to Figure S13 show the histograms of the strain values on both samples at selected heights, as shown in Figure S7. The strain is calculated relative to the lattice constant determined for each dataset from the position of the Bragg peak, as described in Section S7. The data was fitted either by one Gaussian defined as

$$f(x) = a \cdot e^{-(\frac{x-\mu}{\sigma})^2} \tag{S10}$$

with the mean μ and the variance σ^2 or by two Gaussians

$$f(x) = a_1 \cdot e^{-(\frac{x-\mu_1}{\sigma_1})^2} + a_2 \cdot e^{-(\frac{x-\mu_2}{\sigma_2})^2} \tag{S11}$$

In the histogram of the cuts in Sample-150 in which the core-shell structure is visible, one either observes two distinct peaks (f.e. in Figure S8c)) or at least a broadening of the peak (f.e. in Figure S8d)). Both can only be fitted by two Gaussians and not by one.

Figure S14 shows the histogram of all strain values of the initial and final state on each sample. For Sample-150 the width of the histogram is decreasing at the final state compared to the initial state (Figure S14c) compared to a)), while the width

is increasing for Sample-670 (Figure S14d) compared to b)). This broadening of the peak for de-alloyed samples is also reported in literature.[5]

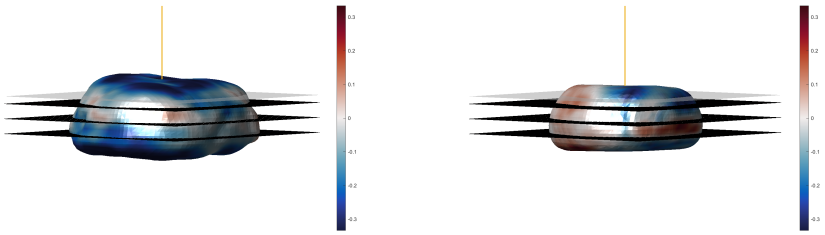

(a) (b)

Fig. S7 Images indicating the planes used to obtain the histograms.
a) Sample-150 inital state with planes indicating the cuts at different heights. b) Sample-670 initial state with planes indicating the cuts at different heights.

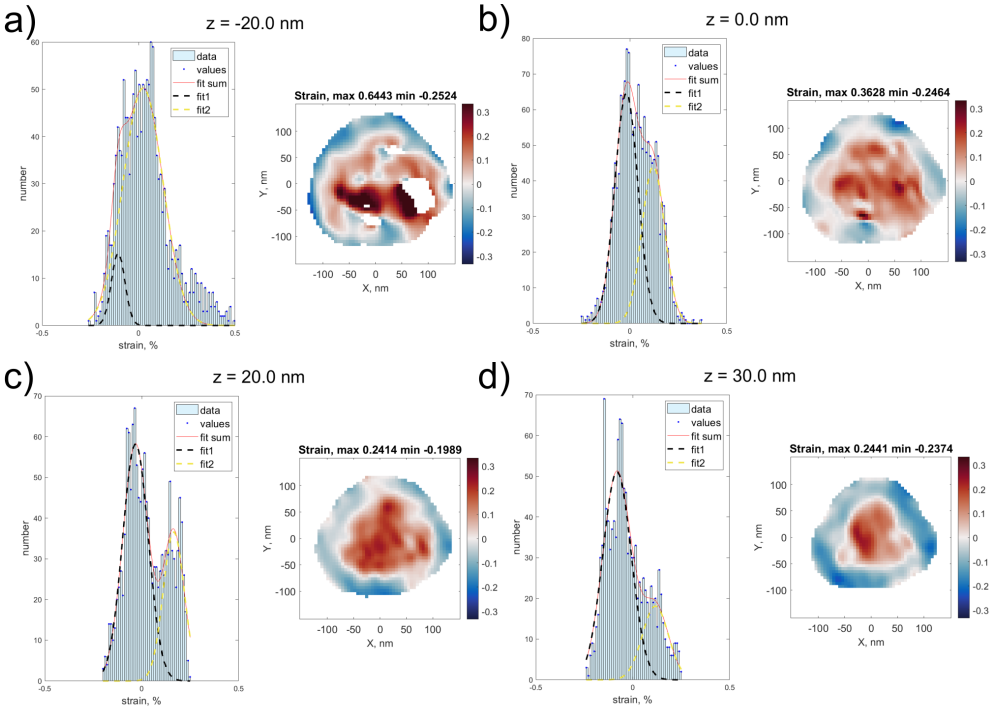

Fig. S8 Histograms of the strain values at different heights, Sample-150 initial state (RT, under Ar atmosphere)
a) Cut at −20 nm, note that a three component fit seems more appropriate. b) Cut at 0 nm, the negative strain peak is fitted to be at -0.018% with $\sigma^2 = 0.007\%$ and the positive strain at 0.121% with σ^2 =0.007%. c) Cut at 20 nm, the negative strain value is fitted to be at -0.032% with σ^2 =0.009% and the positive value at 0.165% with σ^2 =0.006%. d) Cut at 30 nm, the negative strain value is fitted to be at -0.081% with σ^2 =0.011% and the positive strain at 0.117% with σ^2 =0.009%. All histograms are extracted from the first dataset of Sample-150 and fitted by two Gaussian functions, defined as explained in the text. Additionally, the minima and maxima of each plane is written in the sub-image headers of the cuts. The error on the strain values is ±0.088%, see Section S12.

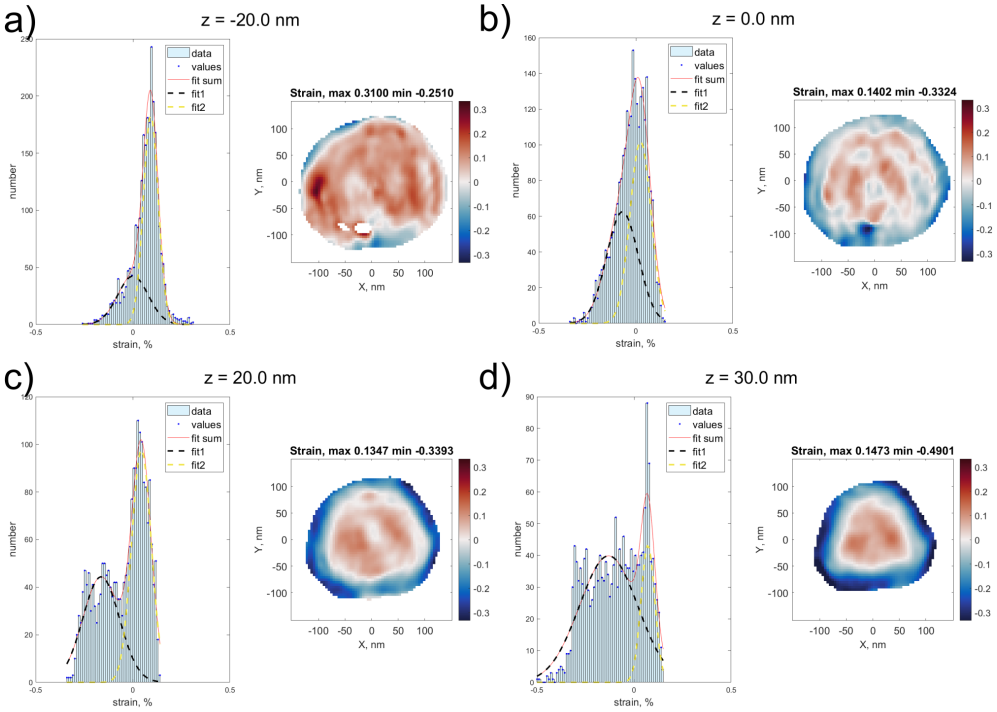

Fig. S9 Histograms of the strain values at different heights, Sample-150 dataset 13 (560 °C under methane oxidation condition)
a) Cut at −20 nm, one strain peak position is fitted to be at 0.000% with σ^2 =0.013% and the positive strain at 0.092% with σ^2 =0.003%. b) Cut at 0 nm the negative strain peak position is fitted to be at -0.069% with σ^2 =0.013% and the positive strain at 0.024% with σ^2 =0.006%. c) Cut at 20 nm the negative strain peak position is fitted to be at -0.163% with σ^2 =0.018% and the positive strain at 0.044% with σ^2 =0.005%. d) Cut at 30 nm. The negative strain peak position is fitted to be at -0.131% with σ^2 =0.045% and the positive strain at 0.071% with σ^2 =0.003%. All histograms are extracted from dataset 13 of Sample-150 and fitted by two Gaussian functions. The error on the strain values is ±0.059%, see Section S12.

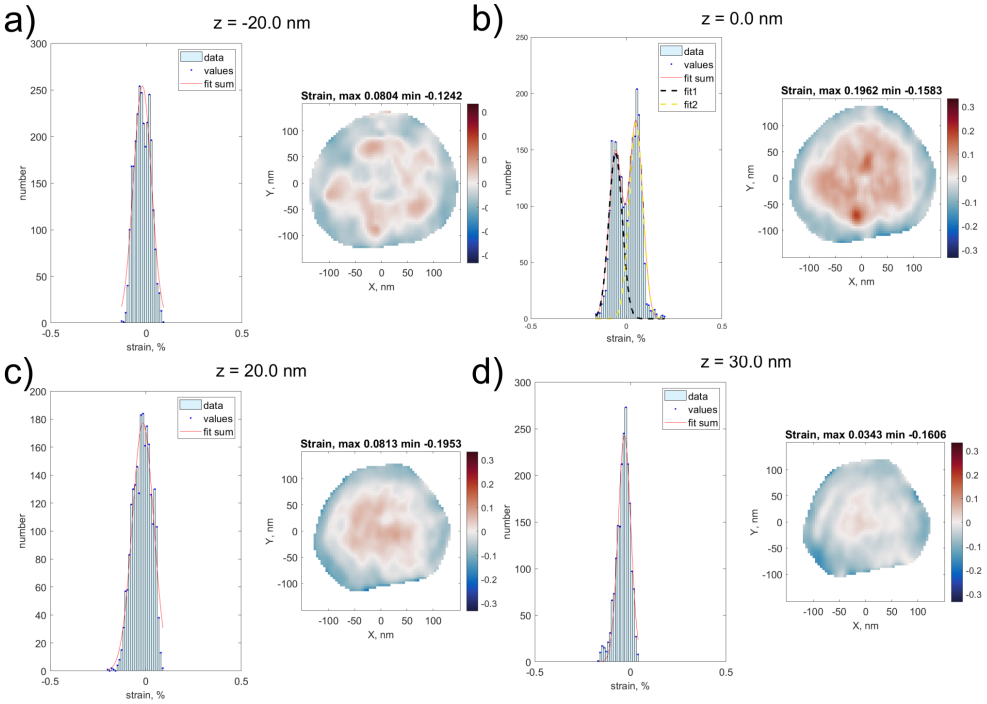

Fig. S10 Histograms of the strain values at different heights, Sample-150 final state (dataset 14, at 620 °C under methane oxidation condition)
a) Cut at −20 nm, the strain peak position is fitted to be at -0.021% with σ^2 =0.005%. b) Cut at 0 nm, the negative strain peak position is fitted to be at -0.057% with σ^2 =0.003% and the positive strain at 0.051% with σ^2 =0.003%. The positive value is smaller compared to the initial state. c) Cut at 20 nm, the strain peak position is fitted to be at -0.015% with σ^2 =0.006%. d) Cut at 30 nm, the strain peak position is fitted to be at -0.031% with σ^2 =0.002%. All histograms from the last dataset on Sample-150 (dataset 14), fitted with Gaussian functions. Besides for b), clearly one Gaussian is more appropriate than two, which is also an indication that the strain values are getting less separated. The error of the strain values is ±0.038%, see Section S12.

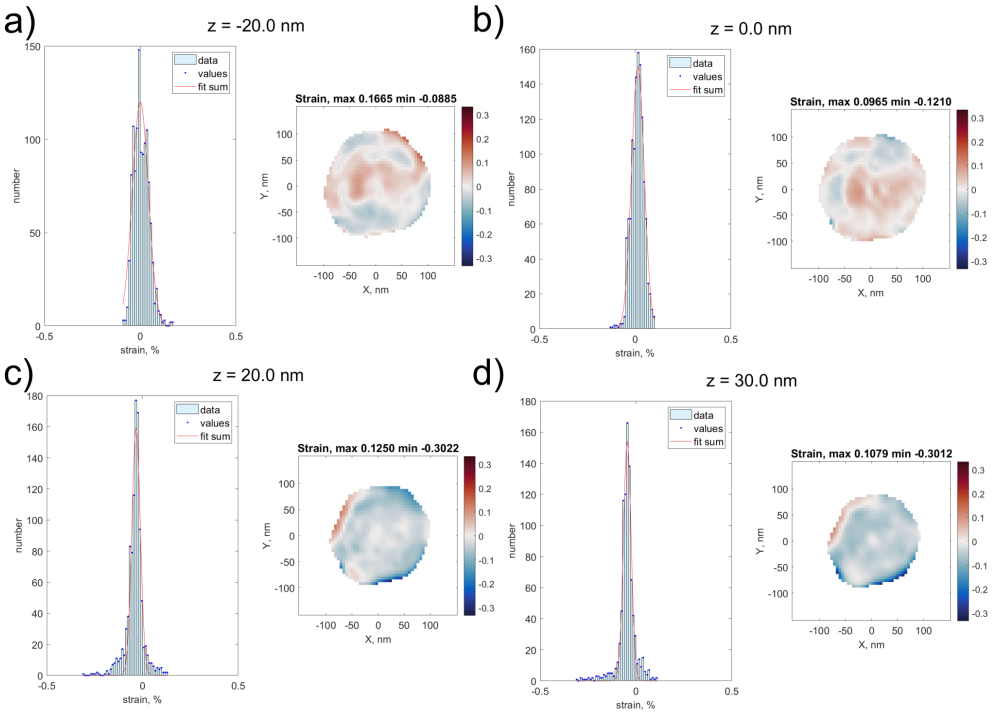

Fig. S11 Histograms of the strain values at different heights, Sample-670 initial state (RT under Ar atmosphere)
Cuts at a) −20 nm with fitted peak position at 0.000% with σ^2 =0.004%, b) 0 nm with fitted peak position at 0.014% with σ^2 =0.002%, c) 20 nm with fitted peak position at -0.033% with σ^2 =0.001% and d) 30 nm with fitted peak position at -0.045% with σ^2 =0.001%. All from the first dataset of Sample-670. The error on the strain values is ±0.049%, as shown in Section S12.

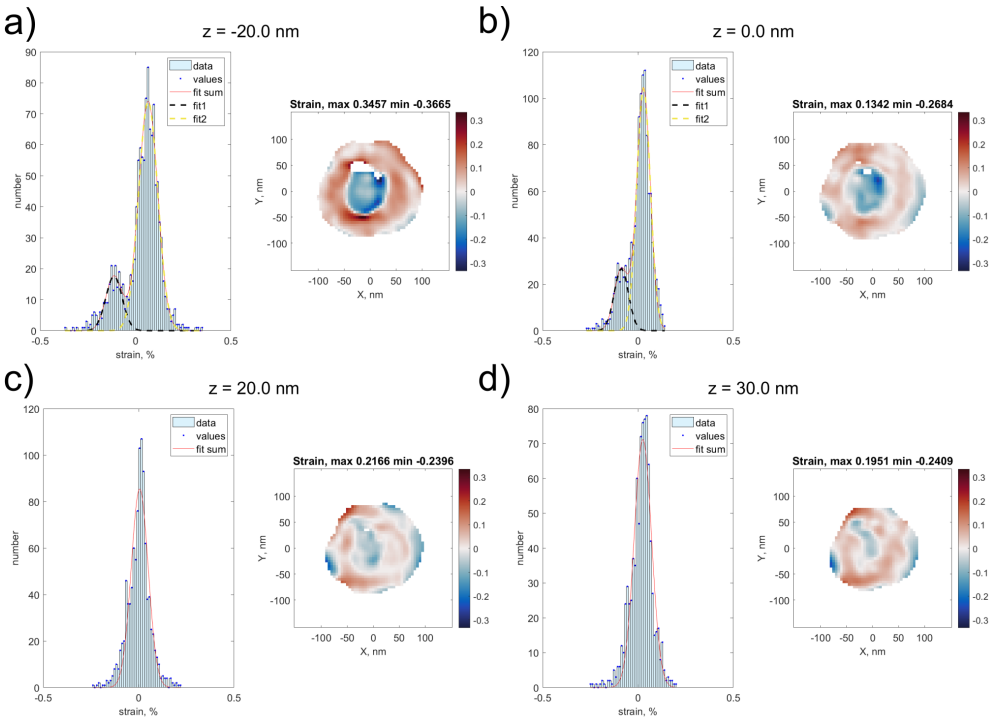

Fig. S12 Histograms of the strain values at different heights, Sample-670 dataset 22 (680 °C **under methane oxidation condition)**
a) Cut at −20 nm with minima of -0.37 and maxima of 0.35%, while the fitted peak positions are at -0.113% with σ^2 =0.004% and 0.066% with σ^2 =0.005%. b) Cut at 0 nm with min: -0.27% max 0.13%, while the fitted peak positions are at -0.087% with σ^2 =0.003% and 0.029% with σ^2 =0.003%. c) Cut at 20 nm with min: -0.24% max 0.22%, while the fitted peak positions is at 0.006% with σ^2 =0.004%. d) Cut at 30 nm with min: -0.24% and max 0.2%, while the fitted peak positions is at 0.025% with σ^2 =0.004%. All from dataset 22 of Sample-670, fitted with one or two Gaussian functions. The error on the strain values is ±0.062%, as shown in Section S12.

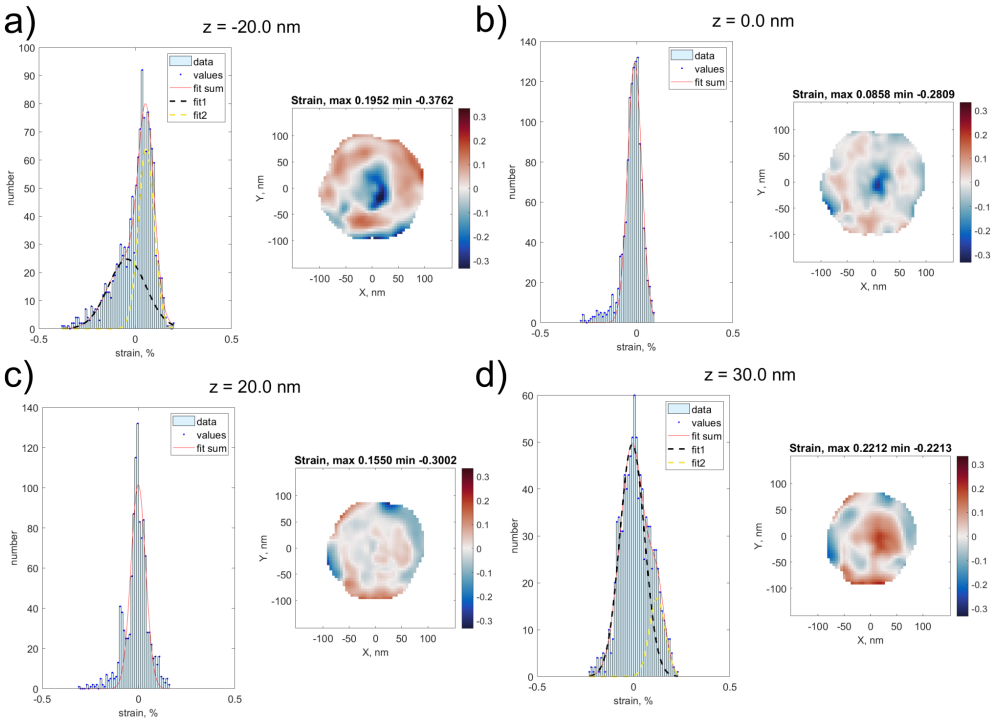

Fig. S13 Histograms of the strain values at different heights, Sample-670 final state (680 °C under methane oxidation condition)
Cut at a) −20 nm with min: -0.37% max 0.19% while the fitted peak positions are at -0.0419% with σ^2 =0.019% and 0.0571% with σ^2 =0.003%. b) 0 nm with min: -0.28 max 0.08% while the fitted peak position is at -0.010% with σ^2 =0.003%. c) 20 nm with min: -0.3% max 0.15% while the fitted peak position is at -0.001% with σ^2 =0.003%. d) 30 nm with min: -0.22% max 0.22% while the fitted peak positions are at -0.007% with σ^2 =0.008% and 0.123% with σ^2 =0.003%. All histograms are created from the last dataset of Sample-670. The error on the strain values is ±0.055%, as shown in Section S12.

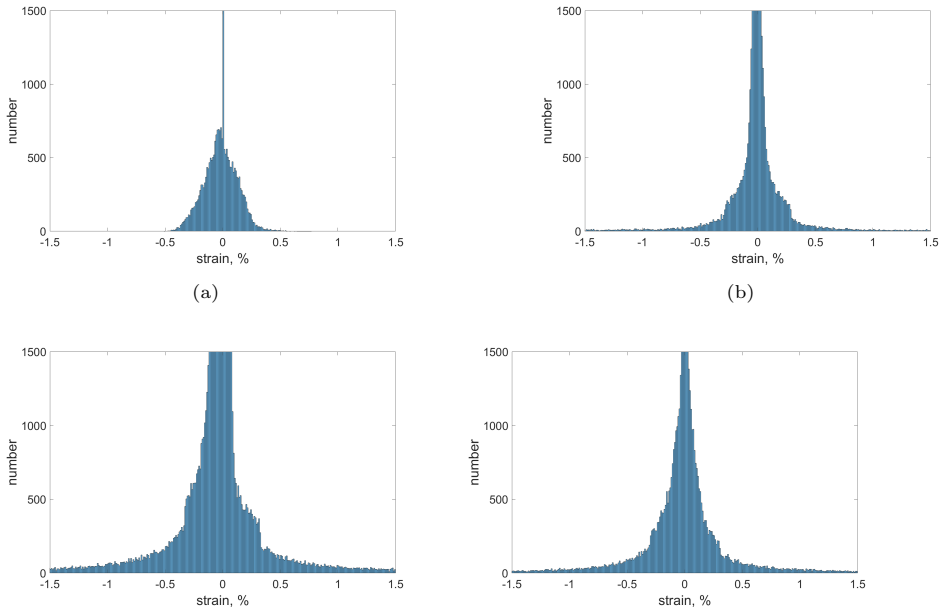

Fig. S14 Histograms of all strain values
a) Sample-150 inital state b) Sample-670 initial state c) Sample-150 final state d) Sample-670 final state

S9 Experimental conditions

Figure S15 and Figure S16 show the experimental conditions including an overview over reconstructions of all datasets for Sample-150 and sample-670, respectively. The gas conditions and temperatures during the BCDI measurements are also listed in Table S6 and Table S7. Since the set-up is not equipped with a massflow controller calibrated for CH_4, the CO massflow controller was used and the flow rate was adapted according to the calculations in Section S15. Due to a mistake in the calculation during the beamtime, the massflow of CH_4 was set to 2.6 mL min^{-1} instead of 1.5 mL min^{-1} to get an total flow of 50 mL min^{-1}.

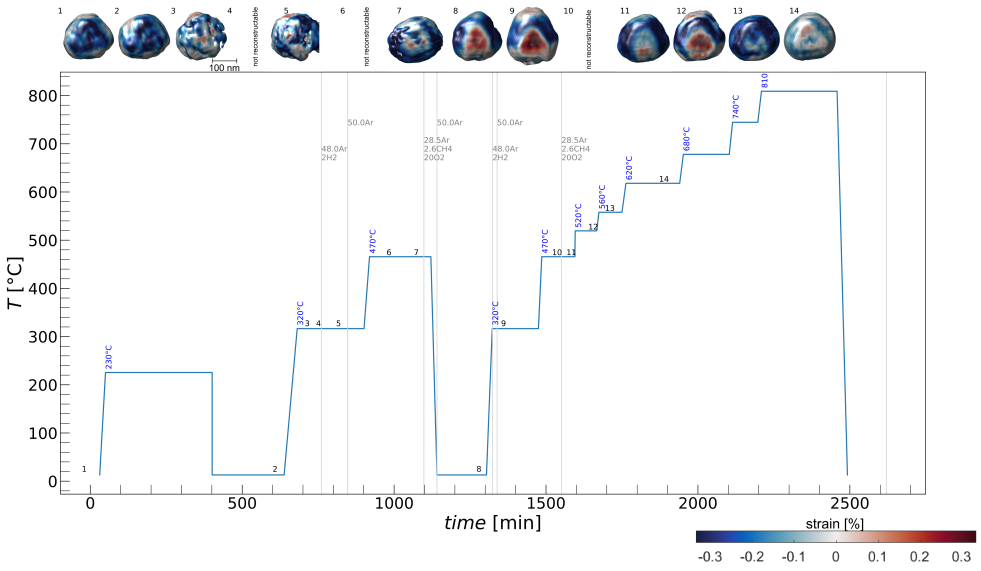

Fig. S15 Overview over the T and the gases on Sample-150
Including a topview on all reconstructions with isosurface value 0.2, besides for dataset 3-7 for which an isosurface value of 0.1 was chosen, as described in Section S16. The colorbar indicates the strain. The gas conditions are given in mL min^{-1}, the black numbers denotes the measured BCDI datasets.

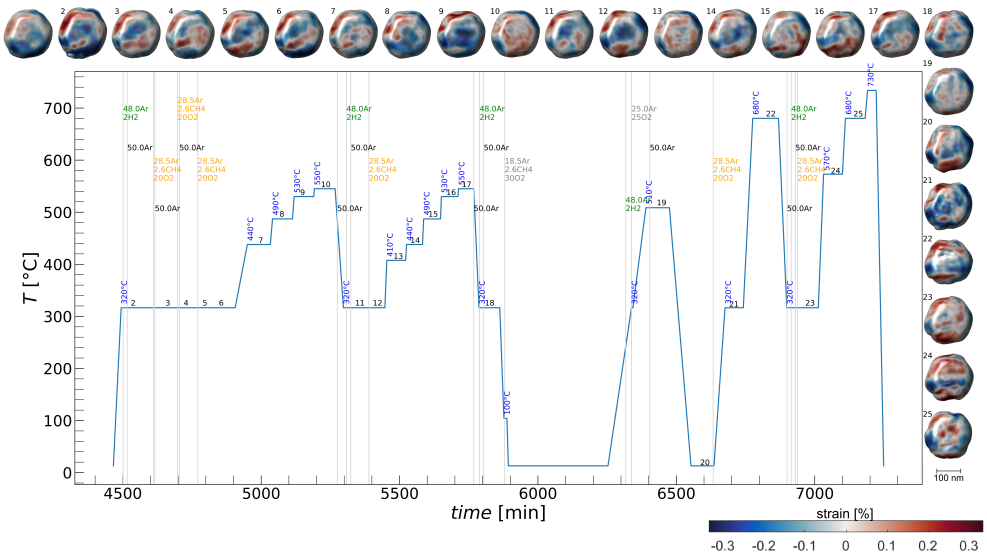

Fig. S16 Overview over the T and the gases in Sample-670
Including a topview on all reconstructions with isosurface value 0.2. The colorbar indicates the strain. The gas tests performed at RT between BCDI dataset 18 and 19 are left out for clarity, all other gas conditions are given in mL min^{-1}. The black numbers denotes the measured BCDI datasets.

Table S6 Experimental conditions of all datasets on Sample-150. Included are only the conditions of the datasets, not the conditions inbetween datasets.

dataset number	T [°C]	gas
1	RT	Ar
2	RT	Ar
3	320	Ar
4	320	Ar
5	320	H2 treatment
6	470	Ar
7	470	Ar
8	RT	Ar
9	320	Ar
10	470	Ar
11	470	methane ox.
12	520	methane ox.
13	560	methane ox.
14	620	methane ox.
15	680	methane ox.

Table S7 Experimental conditions of all datasets on Sample-670. Only included the conditions of the datasets, not the conditions inbetween datasets.

dataset number	T [°C]	gas
1	RT	Ar
2	320	Ar
3	320	methane ox.
4	320	methane ox.
5	320	methane ox.
6	320	methane ox.
7	440	methane ox.
8	490	methane ox.
9	530	methane ox.
10	550	methane ox.
11	320	Ar
12	320	methane ox.
13	410	methane ox.
14	440	methane ox.
15	490	methane ox.
16	530	methane ox.
17	550	methane ox.
18	320	Ar
19	510	Ar
20	RT	Ar
21	320	methane ox.
22	680	methane ox.
23	320	methane ox.
24	570	methane ox.
25	680	methane ox.

S10 Change of lineprofile through fringes

Figure S17 shows the line profiles through the fringes of selected datasets on Sample-670. The increase of the asymmetry indicates the dealloying of the sample.[7] This dealloying is also visible in the detector images in Figure S18. The line profiles are extracted from the datasets as described in Section S5.

The lineprofiles through the fringes of selected datasets on Sample-150 show the opposite trend: the symmetry is slightly increasing, as visible by eye in Figure S19. The detector image at the beginning of the catalysis experiment (Figure S20a)) exhibits a core-shell structure which is clearly changing towards a less strained NP by the end of the experiment in Figure S20b). The development of the fringes can be followed in a selection of detector images in Figure S21.

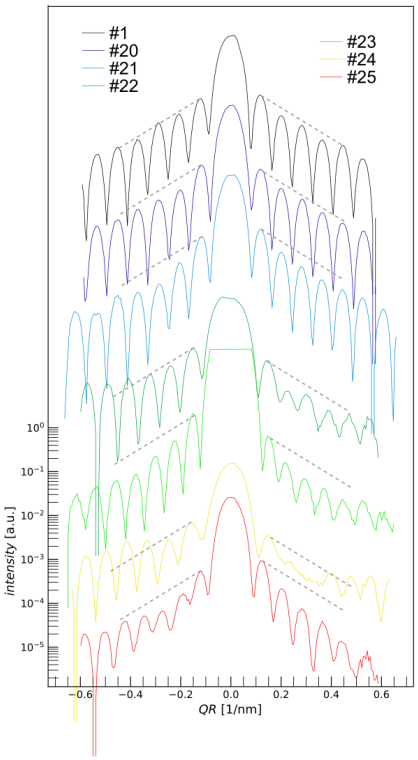

Fig. S17 Line profiles through fringes of selected datasets on Sample-670
Increased asymmetry (higher offset between left and right side, different modulation and different slope) from dataset 21 to 22, which is indicating the dealloying, as described in [7]. All gray dotted lines have the same slope.

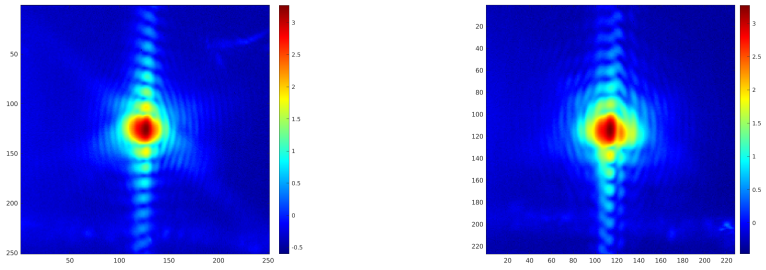

(a) (b)

Fig. S18 Selected stacked detector images of Sample-670
a) Dataset 21 and b) dataset 22. All stacked detector images are shown in Section S6. The 'splitting' of the fringes in detector images indicate core-shell structures.[6].

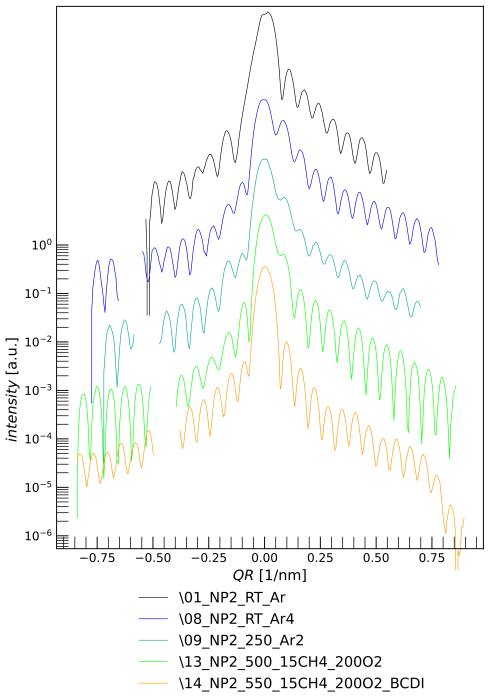

Fig. S19 Lineprofiles through fringes of selected datasets on Sample-150
They show a slight decreasing asymmetry over the course of the experiment. Especially from dataset 13 to 14, the offset between left and right side is reduced, which is indicating the start of the alloying, as described in [7].

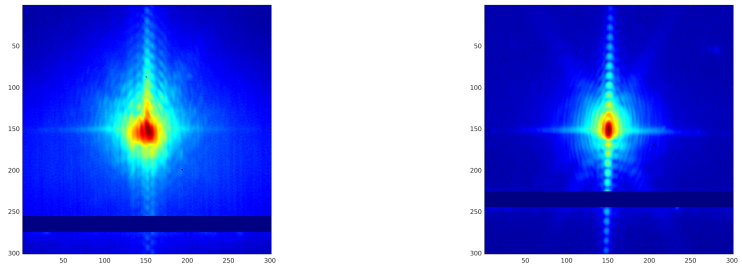

(a) (b)

Fig. S20 Selected stacked detector images of Sample-150
a) Dataset 1 b) dataset 14. The detector images indicate a core-shell structure for dataset 1, see [6].

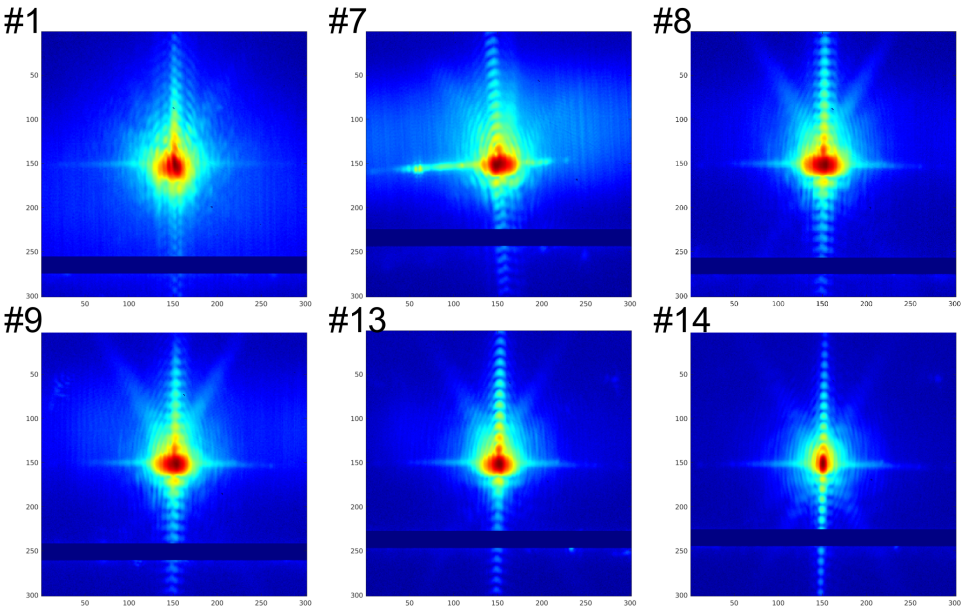

Fig. S21 Stacked detector images of selected datasets on Sample-150
Clearly the intensity distribution is changing over the course of the experiment. The displayed images have the same range around the Bragg peak for all datasets, other than the ROIs used for reconstruction. ROIs chosen for reconstruction are displayed in Figure S4.

S11 Radius of half-sphere of overgrown Pd

To confirm that Sample-670 was overgrown with sufficient Pd to fill the volume of the compressive strain region of the NP in dataset 22, we estimate the volume of the overgrown Pd. Therefore we assume a perfect hexagonal topfacet of the NP, so that we can calculate the volume of the overgrown Pd with $V_{\mathrm{Pd}} = A \cdot h = 2\sqrt{3}r^2h$, as we did in Section S4. Thereby, the height h is equal to the nominal thickness of 5 nm overgrown Pd. With $V_{\mathrm{Pd}} \stackrel{!}{=} V_{\text{half-sphere}}$ it follows, that the volume would be sufficient to fill a half-sphere of $V_{\text{half-sphere}} = 4/6\pi r^3_{\text{half-sphere}}$ with radius $r_{\text{half-sphere}} = 42$ nm. This agrees (within the errorbars) to the radius $r = 40 \pm 5$ nm of the area with the compressive strain in datset 22 cut at -20 nm.

S12 Strain error

The systematic absolute error of the strain values was estimated by calculating the strain independently for all ten reconstructions selected for averaging. Afterwards, calculating the standard deviation of the ten reconstructions at each point inside the NP. Then all standard deviations were averaged to get the error bar for the strain of one dataset.

This error does not include the error from reading the Bragg peak position for the calculation of the lattice constant. That is described in Section S7.

Table S8 Overview over the absolute strain error of all datasets on Sample-150. Additionally, the table contains the lattice constant a_{NP} which was used to calculate the strain. The lattice constant was determined from the Bragg peak position, as described in S7.

dataset number	strain error	a_{NP} [Å]
1	±0.088%	3.920
2	±0.083%	3.920
3	±0.122%	3.932
4	-	-
5	±0.121%	3.932
6	-	-
7	±0.131 %	3.937
8	±0.074%	3.920
9	±0.078%	3.932
10	±0.083%	3.938
11	±0.073%	3.937
12	±0.091%	3.939
13	±0.059%	3.942
14	±0.038%	3.944
15	-	-

Table S9 Overview over the absolute strain error for all datasets on Sample-670. Additionally, the table contains the lattice constant a_{NP} which was used to calculate the strain. The lattice constant was determined from the Bragg peak position, as described in S7.

dataset number	strain error	a_{NP} [Å]
1	±0.049%	3.920
2	±0.035%	3.931
3	±0.033%	3.931
4	±0.04%	3.930
5	±0.045%	3.930
6	±0.049%	3.930
7	±0.039%	3.935
8	±0.041%	3.938
9	±0.042%	3.942
10	±0.036%	3.940
11	±0.028%	3.931
12	±0.035%	3.930
13	±0.037%	3.934
14	±0.046%	3.935
15	±0.029%	3.937
16	±0.036%	3.939
17	±0.030%	3.939
18	±0.033%	3.931
19	±0.027%	3.938
20	±0.043%	3.920
21	±0.028%	3.930
22	±0.063%	3.944
23	±0.036%	3.930
24	±0.049%	3.940
25	±0.055%	3.944

S13 Critical thickness

The critical thickness was calculated by

$$h_{\mathrm{c}} = \frac{a_{\mathrm{Pd}}}{2\pi \cdot f} \frac{1 - \nu \cdot cos^2(\alpha)}{(1+\nu) \cdot cos(\lambda)} (ln(\frac{h_{\mathrm{c}}}{a_{\mathrm{Pd}}}) + 1) \tag{S12}$$

with the lattice constant a_{Pd} of Pd, the Poisson value $\nu = 0.39$ of Pd, the missfit $f = (a_{\mathrm{Pt}} - a_{\mathrm{Pd}})/a_{\mathrm{Pd}} = 0.85$, $cos(\lambda) = 0.5$ and $cos^2(\alpha) = 0.25$.[8] This model is assuming a stiff substrate.

S14 Temperature calibration

The sample was heated using a graphite/boronitride resistance heater. A calibration measurement was performed to correlate the applied currents to the temperature. This calibration was done under 50 mL/min Ar with 0.1 bar on a Nb doped STO substrate with identical thickness (0.5 mm) and the same YSZ spacer (1.5 mm) as used during the *in situ* experiment at P10. The temperature was measured by a pyrometer with emissivity $\epsilon = 0.85$ and the results are shown in Figure S22. Throughout the analysis of the *in situ* experiment the temperatures T were calculated from the current I by $T = 303.6 \cdot I + 12.94$ for currents up to 1.47 A and $T = 214.55 \cdot I + 143.88$ for currents above. The temperatures were rounded to the nearest ten.

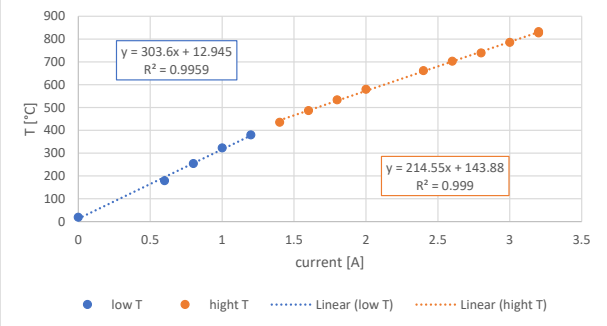

Fig. S22 Temperature calibration
The measured temperatures were fitted by two linear fits, which cross at 1.47 A. R^2 specify the errors of the fits.

S15 Calculation of real flow

CH_4 was flown in a massflow controller which was calibrated for CO. To get the real flow F_{real} from the flow which was set in the software F_{set}, the following equation was used:

$$F_{\text{real}} = \frac{F_{\text{set}}}{\frac{HC_{\text{MFC gas}}}{HC_{\text{real gas}}} \cdot \frac{\rho_{\text{MFC gas}}}{\rho_{\text{real gas}}}} \tag{S13}$$

with the heat capacities HC and the density ρ of the real gas (here CH_4) and of the gas for which the MFC was calibrated (here CO).

The following values were taken from [1] and used for calculation:

For CH_4: $HC_{CH_4} = 0.568$, $\rho_{CH_4} = 0.7175$

For CO: $HC_{CO} = 0.249$, $\rho_{CO} = 1.25$

S16 Choosing isosurface value

For Sample-150 several isosurface values were tested on multiple datasets to choose the best one, as shown in Figure S23 to Figure S27. We decided to use an isosurface value of 0.2, since it looks the most reasonable for dataset 1, 9 and 14. Only for datasets 3-7, an isosurface value of 0.1 was chosen, since for those datasets, the reconstructed shapes have holes otherwise. Even after choosing the best from over 250 single reconstructions, the result could not be improved for dataset 3 to 7.

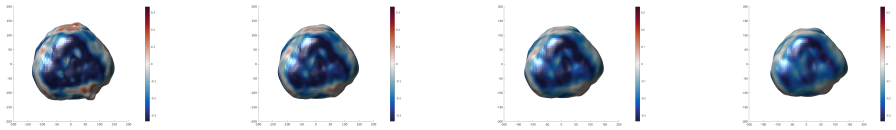

(a) (b) (c) (d)

Fig. S23 Testing different isosurface values for dataset 1
with a) 0.1 b) 0.15 c) 0.2 and d) 0.3, the colorbar represents the strain in %.

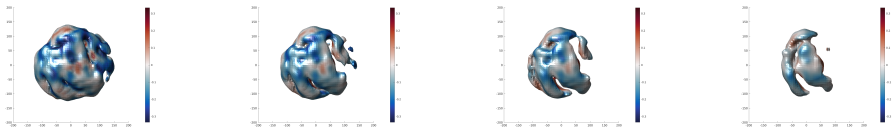

(a) (b) (c) (d)

Fig. S24 Testing different isosurface values for dataset 3
with a) 0.1 b) 0.15 c) 0.2 and d) 0.3, the colorbar represents the strain in %.

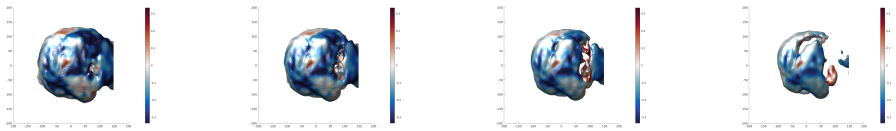

(a) (b) (c) (d)

Fig. S25 Testing different isosurface values for dataset 5
with a) 0.1 b) 0.15 c) 0.2 and d) 0.3, the colorbar represents the strain in %.

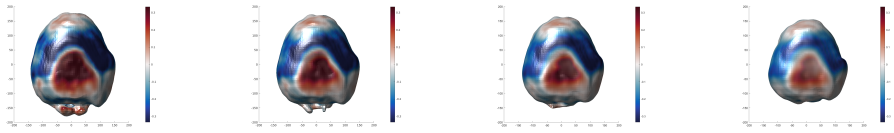

(a) (b) (c) (d)

Fig. S26 Testing different isosurface values for dataset 9
with a) 0.1 b) 0.15 c) 0.2 and d) 0.3, the colorbar represents the strain in %.

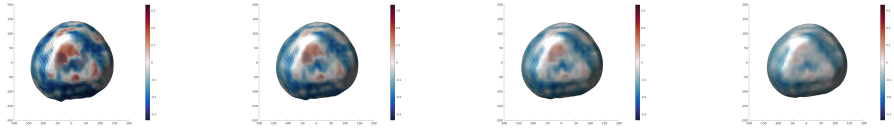

(a) (b) (c) (d)

Fig. S27 Testing different isosurface values for dataset 14
with a) 0.1 b) 0.15 c) 0.2 and d) 0.3, the colorbar represents the strain in %.

References

[1] (2006) Digital Mass Flow Controller Type 1579A and Digital Mass Flow Meter 579A - Instruction Manual. MKS Instruments Deutschland GmbH, 1st edn., available at https://www.mpi-hd.mpg.de/gerda/TG04_TECHNICAL/manuals/1579A_EN_0601.pdf

[2] Arblaster JW (1997) Crystallographic properties of platinum. Platinum Metals Review 41:12–21

[3] Arblaster JW (2012) Crystallographic properties of palladium. Platinum Metals Review 56:181–189

[4] Baheti VA, Ravi R, Paul A (2013) Interdiffusion study in the pd–pt system. J Mater Sci: Mater Electron 24:2833–2838

[5] Cha W, Liu Y, You H, et al (2017) Dealloying in Individual Nanoparticles and Thin Film Grains: A Bragg Coherent Diffractive Imaging Study. Adv Funct Mater 27:1700331

[6] Chatelier C, Atlan C, Dupraz M, et al (2024) Unveiling coreshell structure formation in a ni3fe nanoparticle with in situ multi-bragg coherent diffraction imaging. ACS Catal 18:13517 – 13527

[7] Haag ST, Richard MI, Labat S, et al (2013) Anomalous coherent diffraction of coreshell nano-objects: A methodology for determination of composition and strain fields. Phys Rev B 87:035408

[8] Matthews JW, Blakeslee AE (1974) Defects in epitaxial multilayers. Journal of Crystal Growth 27:118–125

[9] Shewmon P (1989) Diffusion in Solids. Wiley, New York